Streamwise variation of turbulent dynamics in boundary layer flow of drag-reducing fluid

Shinji Tamano, Michael D. Graham and Yohei Morinishi

Journal of Fluid Mechanics / Volume 686 / November 2011, pp 352 - 377
DOI: 10.1017/jfm.2011.334, Published online: 22 September 2011

J. Fluid Mech. (2011), *vol.* 686, *pp.* 352–377.
doi:10.1017/jfm.2011.334

Streamwise variation of turbulent dynamics in boundary layer flow of drag-reducing fluid

Shinji Tamano[1,2]†, Michael D. Graham[2] and Yohei Morinishi[1]

Graduate School of Engineering, Nagoya Institute of Technology, Gokiso-cho, Showa-ku, Nagoya, Aichi 466-8555, Japan

Department of Chemical and Biological Engineering, University of Wisconsin–Madison, Madison, WI 53706-1607, USA

(Received 28 January 2011; revised 1 July 2011; accepted 1 August 2011; first published online 22 September 2011)

Direct numerical simulations (DNSs) of a zero-pressure-gradient boundary layer flow of a polymeric fluid have been performed. The FENE-P model was used for the polymer stresses and a wide range of Weissenberg numbers (*We*) was addressed. In all cases, the streamwise variations of the level of polymer stretching and the level of drag reduction are anticorrelated. Consistent with earlier studies, the inlet condition for the flow consists of Newtonian velocity data with no polymer stretching, so in the upstream region of the boundary layer the polymer molecules stretch strongly in response, leading to an initial spatial maximum in polymer stretching. Beyond this initial region, the level of drag reduction increases with increasing downstream position, while the polymer stretch is decreasing. At sufficiently high Weissenberg numbers, these variations are monotonic with streamwise position (outside the upstream region), but at $We = 25$, both the polymer stretching and level of drag reduction display a decaying oscillation in the downstream position. The streamwise dependence of the velocity statistics is also shown. In addition, simulations in which the polymer stress is turned off beyond a chosen downstream position were performed; in this case the flow continues to exhibit substantial drag reduction well downstream of the cutoff position. These observations are analysed in light of other recent literature and in particular the observations of 'active' and 'hibernating' turbulence recently found in minimal channel flow by Xi and Graham. All of these observations suggest that an important role for viscoelasticity in the turbulent drag reduction phenomenon, at least near solid surfaces, is to suppress conventional turbulence, while leaving behind a much weaker form of turbulence that can persist for a substantial length of time (or downstream distance) even in the absence of viscoelastic stresses.

Key words: drag reduction, polymers, turbulent boundary layers

1. Introduction

It is well known that significant drag reduction can be observed for wall-bounded turbulent flows of viscoelastic fluids such as dilute polymer and surfactant solutions. A key result in the literature of drag reduction was obtained by Virk (1975) who noted the existence of a parameter regime called the maximum drag reduction

† Email address for correspondence: tamano.shinji@nitech.ac.jp

(MDR) asymptote. In this regime the mean velocity profile has a log-law region with a distinct slope that is universal with respect to molecular weight, concentration, polymer species, and pipe diameter. It has been reported that in the MDR regime the Reynolds shear stress substantially decreases (Warholic, Massah & Hanratty 1999*a*; Warholic, Schmidt & Hanratty 1999*b*). The Virk mean velocity profile in the MDR regime has been reproduced by direct numerical simulations (DNSs) of drag-reducing turbulent channel flow of polymer solutions (e.g. Ptasinski *et al.* 2003; Dubief *et al.* 2005; Li, Sureshkumar & Khomami 2006).

However, despite numerous efforts in this field (e.g. Virk 1975; Sreenivasan & White 2000; Benzi, De angelis & L'vov 2006; Procaccia, L'vov & Benzi 2008), understanding of MDR remains largely phenomenological or empirical (White & Mungal 2008). Since the pioneering papers of Sureshkumar, Beris & Handler (1997) and Dimitropoulos *et al.* (2005) on the DNS of the drag-reducing channel flow and boundary layer, respectively, numerous DNS studies have been performed to investigate the viscoelastic wall-bounded turbulent flows using constitutive equation models such as the finitely extensible nonlinear elastic Peterlin (FENE-P) model, Oldroyd-B model and Giesekus model (Bird, Armstrong & Hassager 1987*a*,*b*). As reported in the review of White & Mungal (2008), these studies can predict some experimental findings such as a steeper gradient of the mean velocity profile in wall units and more suppression of wall-normal turbulence intensity and Reynolds shear stress with the amount of the drag reduction, and have revealed the effect of viscoelastic stress on velocity fields.

More specifically, DNS studies on drag-reducing turbulent channel flows indicate that the elongational viscosity and Weissenberg number are key parameters for the drag reduction (e.g. Dimitropoulos, Sureshkumar & Beris 1998; Housiadas & Beris 2004; Li *et al.* 2006; Yu & Kawaguchi 2003, 2006). At a constant Weissenberg number, moreover, Tamano *et al.* (2009*a*) performed DNS of the drag-reducing turbulent boundary layer in viscoelastic fluids using the Oldroyd-B, Giesekus and FENE-P models, and clarified the effects of rheological properties such as the elongational and shear viscosities, and the first and the second normal stress differences on the drag reduction. Owing to these macroscopic approaches, substantial new knowledge on the relation between the drag reduction and rheological properties of viscoelastic solutions such as the relaxation time and elongational viscosity has been obtained. In terms of relation between polymer stress and turbulence structures, moreover, many researchers showed that polymer stresses counteract near-wall streamwise vortices (e.g. De Angelis, Casciola & Piva 2002; Stone, Waleffe & Graham 2002; Stone *et al.* 2004; Dubief *et al.* 2004, 2005; Li & Graham 2007; Kim *et al.* 2007, 2008). However, how polymers or surfactant micelles interact with near-wall turbulence structure, especially as the level of drag reduction approaches the MDR regime, remains poorly understood.

Xi & Graham (2010*a*,*b*) have recently studied Newtonian and viscoelastic turbulent dynamics in a minimal channel flow geometry. A number of the observations from that study are relevant to the present work. The main overall observation Xi & Graham (2010*b*) was the existence of time intervals of what they called 'hibernating' turbulence, during which the polymer stresses decreased while the mean velocity was increasing. During hibernation, the instantaneous mean velocity profile approached a log-law with a slope approaching that found in the MDR regime, and the Reynolds shear stresses, streamwise vortex strength and streamwise variation of the flow field all dropped to low values. Under the conditions considered, these hibernation intervals last about five eddy turnover times, after which the turbulence reverts to a more

conventional, 'active' state. As the Weissenberg number increases, the active intervals become shorter, while the hibernating intervals remain approximately the same length. Thus, a key result of this paper is that in the minimal channel, the instantaneous levels of polymer stretching and drag reduction are anticorrelated in time: during the active turbulence intervals, the polymers become highly stretched and the resulting stresses suppress the active turbulence, driving the flow into hibernation. During hibernation, the turbulence is very weak and does not stretch the polymer molecules, which therefore relax. The hibernating turbulence is unstable and eventually new three-dimensional turbulent fluctuations grow, moving the turbulence back into the active regime. Finally, another key result of this study was that intervals of hibernation displaying the Virk slope are observed even in the limit of zero Weissenberg number: Newtonian flow. One key goal of the present work is to determine to what extent the anticorrelation of polymer stretching and drag reduction observed in the minimal channel results is found in boundary layer turbulence.

There is some existing evidence that this scenario is relevant, with time replaced with downstream position, for boundary layer flow. Dimitropoulos *et al.* (2005) found that drag reduction increases as polymer extension decreases. Dimitropoulos *et al.* (2005) and Hou, Somandepalli & Mungal (2008) also proposed that in the steady-state region, the reduced turbulent intensity allowed the polymer to be less stretched and still maintained a high drag reduction, so that the polymer stress was not necessarily high. As reported by Hou *et al.* (2008), the dependence of turbulence intensity of the velocity fluctuations on the drag reduction ratio is more complex compared with the turbulent channel flow. Very recently, Dubief *et al.* (2011) observed, in a simulation of Newtonian boundary layer flow, that at a spatial position just upstream of where streamwise vortices and turbulent spots form the mean velocity profile looks strikingly similar to the Virk MDR profile. This observation is further evidence of the transient presence of MDR-like dynamics in Newtonian flow.

In the present study, we perform DNS of a zero-pressure gradient turbulent boundary layer of a drag-reducing homogeneous viscoelastic fluid with the FENE-P model at Weissenberg numbers up to $We = 100$, and investigate the effects of We on streamwise variations in turbulence statistics and structures in the turbulent boundary layer. Although there have been some past comparisons of turbulence statistics at $We = 25$ and 50 for the boundary layer (see Dimitropoulos *et al.* 2005; Tamano *et al.* 2009*a*), the literature on the effect of We on turbulence structures is very limited in comparison to channel flow. In particular, the modification of streamwise variations remains unknown. In the present study, the streamwise computational domain is enlarged by a factor of two compared with our previous DNS at $We = 25$ (Tamano *et al.* 2007). A particular focus of this work is the evaluation of the results in light of the observations of active and hibernating turbulence in channel flow and their relevance in the more complex case of boundary layer flow.

The present paper is arranged as follows. The fundamental equations and numerical methods are presented in §§ 2 and 3. In § 4, numerical simulation results are presented. First, the effect of We on turbulence statistics and their streamwise variations are investigated. Next, the joint probability density functions of instantaneous wall-shear stress (or trace of conformation tensor) and streamwise velocity scaled by friction velocity at a constant wall-normal position are discussed. Finally, the results of additional numerical simulations at $We = 100$ with a damping function which makes all components of conformation tensor zero in the downstream region are presented in order to clarify the role of conformation tensor. Throughout, we assess the relevance of

the active–hibernating picture for the boundary layer flow. Key results are summarized and conclusions are given in § 5.

2. Formulation

The non-dimensional continuity and momentum equations for incompressible viscoelastic flow are

$$\frac{\partial u_i}{\partial x_i} = 0, \tag{2.1}$$

$$\frac{\partial u_i}{\partial t} + \frac{\partial u_i u_j}{\partial x_j} = -\frac{\partial p}{\partial x_i} + \frac{1-\beta}{Re_{\theta_0}}\frac{\partial E_{ij}}{\partial x_j} + \frac{\beta}{Re_{\theta_0}}\frac{\partial^2 u_i}{\partial x_j \partial x_j}, \tag{2.2}$$

where u_i is the velocity component, p is pressure, x_i is a spatial coordinate, t is time and E_{ij} is the viscoelastic stress component. In this paper, x_1 (x), x_2 (y) and x_3 (z) directions are streamwise, wall-normal and spanwise, respectively. In the present study, the non-dimensional computational parameters are the momentum–thickness Reynolds number Re_{θ_0} and the Weissenberg number We, which are defined as follows:

$$Re_{\theta_0} = \frac{\rho U_e \theta_0}{\eta_0}, \tag{2.3}$$

$$We = \frac{\lambda U_e}{\theta_0}, \tag{2.4}$$

where U_e is the free stream velocity, θ_0 is the momentum–thickness at the inlet plane of the driver part, ρ is density and λ is the relaxation time. The ratio of solvent viscosity η_s to zero shear rate solution viscosity η_0 is β. The non-dimensional FENE-P constitutive equation for the conformation tensor C_{ij} is as follows (Bird *et al.* 1987*b*):

$$\frac{\partial C_{ij}}{\partial t} + u_k \frac{\partial C_{ij}}{\partial x_k} - \frac{\partial u_i}{\partial x_k} C_{kj} - \frac{\partial u_j}{\partial x_k} C_{ik} = -E_{ij}. \tag{2.5}$$

The viscoelastic stress is related to the conformation tensor as

$$E_{ij} = \frac{f C_{ij} - \delta_{ij}}{We}, \tag{2.6}$$

where the Peterlin function f is defined by

$$f = \frac{L^2}{L^2 - \mathrm{Tr}(C_{ij})}, \tag{2.7}$$

and L represents the maximum extension of the polymer. For the FENE-P model, the extensibility parameter Ex is given by

$$Ex = \frac{2L^2(1-\beta)}{3\beta}. \tag{2.8}$$

This is the maximum value of the ratio between polymeric and viscous contributions to extensional viscosity (Trouton ratio). Only when the extensibility parameter Ex is much larger than unity are significant effects of the polymer on turbulence expected. In the present study, in which β and L^2 are fixed at 0.9 and 10 000, respectively, the value of Ex is 740.74.

In this study, the inflow condition for the boundary layer is given by the method proposed by Lund, Wu & Squires (1998), so that the computational domain is divided

into the main part and driver part from which the inflow condition for the main part is obtained. This approach was also used in prior studies (Dimitropoulos *et al.* 2005, 2006; Tamano *et al.* 2007, 2009*a*). The inlet boundary condition is discussed further in the next section.

3. Numerical method and conditions

The second-order accurate finite difference scheme on a staggered grid is used. The velocity components are discretized on the grid cell edges, whereas the pressure and all components of the viscoelastic stress tensor E_{ij} and conformation tensor C_{ij} are defined at the centre of each cell. The coupling algorithm of the discrete continuity and momentum equations (2.1) and (2.2) is based on the second-order splitting method (Dukowicz & Dvinsky 1992). The resulting discrete Poisson equation for the pressure is solved by the Bi-CGSTAB (bi-conjugate gradients stabilized) method (Van Der Vorst 1992) after fast Fourier transform (FFT) in the periodic (z) direction. The second-order upwind difference scheme is used for the polymer-stress convection term $u_k \partial C_{ij}/\partial x_k$ in (2.5). An artificial diffusion term $1/(ScRe_{\theta_0})\partial^2 C_{ij}/\partial {x_j}^2$ is added in (2.5) to prevent numerical instability, where $Sc = \eta_0/(\rho D)$ is the Schmidt number and D is an artificial stress diffusion coefficient for polymer. (Using the actual, very small value of the molecular diffusivity would not lead to stabilization.) The semi-implicit time marching algorithm is used where the diffusion term in the wall-normal direction is treated implicitly with the Crank–Nicolson scheme, and the third-order Runge–Kutta scheme is used for all other terms.

The non-slip boundary condition ($u = v = w = 0$) is applied on the wall. The boundary conditions on the top surface of the computational domain are $\partial u/\partial y = 0$, $v = U_e \, \mathrm{d}\delta^*/\mathrm{d}x$, and $\partial w/\partial y = 0$, where δ^* is the boundary layer displacement thickness. Periodic boundary conditions for the velocity and viscoelastic stress components are imposed in the spanwise direction. A convective boundary condition, $\partial u_i/\partial t + U_e \partial u_i/\partial x = 0$, is used at the outlet plane. The inflow condition is generated using the recycle method of Lund *et al.* (1998) as mentioned above. This is because otherwise, a very long streamwise computational domain would be necessary to capture the spatially developing boundary layer flow including the laminar to turbulent transition Wu & Moin (2009). Simulating this entire region would be extremely computationally expensive. In the present study, the velocity field data at the streamwise centre of the driver part provide inflow data at the inlet of the main part. The present inlet boundary conditions are the same as those of previous studies (Dimitropoulos *et al.* 2005, 2006; Tamano *et al.* 2007, 2009*a*). The boundary conditions for the viscoelastic stress components are given by solving the constitutive equations at the wall with the velocity boundary conditions satisfied, except for the inlet boundary of the main part at which all of the viscoelastic stress components E_{ij} are fixed at zero, i.e. the Newtonian velocity data are imposed directly. It is known that this type of inlet boundary condition has consequences for the predicted level of the drag reduction and the polymer conformation state near the inlet region. In particular, the polymer molecules stretch rapidly from their equilibrium state and the resulting large extensional viscosity leads to an initial increase in drag relative to the Newtonian flow, and thus to a negative level of drag reduction (see figures 3 and 10*b*). Physically, the imposed inlet condition is somewhat analogous to injecting the polymer into a boundary layer at a finite distance downstream from the leading edge.

In the present study, the momentum–thickness Reynolds number Re_{θ_0} is 500 and the Weissenberg number $We = 25$, 50, 75 and 100 (see table 1). The size of the

	We	β	L^2	$\Delta tU_e/\theta_0$
Newtonian	—	1.0	—	0.020
FENE-P	25, 50, 75, 100	0.9	10 000	0.008

TABLE 1. Numerical and physical conditions.

We	$T_{residence}/\lambda$	$T_{integral}/\lambda$
25	16.0	80
50	8.0	40
75	5.3	27
100	4.0	20

TABLE 2. Residence and integral time versus relaxation time.

computational domain for the present simulations is equal to $(L_x \times L_y \times L_z) = (400\theta_0 \times 30\theta_0 \times 20\pi\theta_0/3)$ in the streamwise, wall-normal and spanwise directions, respectively. The grid size is $(N_x \times N_y \times N_z) = (512 \times 64 \times 64)$. The grid spacing in x and z directions is uniform, and the wall-normal grids are given by a hyperbolic tangent stretching function. The present spatial resolution is $(\Delta x^+|_{inlet}, \Delta y^+_{min}|_{inlet} - \Delta y^+_{max}|_{inlet}, \Delta z^+|_{inlet}) = (20, 0.38\text{–}37, 8.5)$ for both Newtonian and the FENE-P model, which is somewhat larger than that of previous DNSs (Dimitropoulos *et al.* 2005, 2006) for the corresponding drag-reducing turbulent boundary layer with the same spatial discretization method. Recent high-resolution spectral DNSs for Newtonian flows showed surprisingly large differences in both basic integral quantities such as the friction coefficient and the shape factor, and revealed that the numerical simulation of turbulent boundary layers was, mainly due to the spatial development of the flow, very sensitive to, for example, proper inflow condition, sufficient settling length and appropriate box dimensions (see Schlatter & Örlü 2010). The present numerical gird resolution is not enough to compare quantitatively such recent spectral DNS results for Newtonian flows, but it is not expected to affect the qualitative conclusions obtained in the present study on the drag-reducing effects (see also § 4.1 for details). The streamwise and spanwise computational sizes in wall units at the inlet are $L_x^+|_{inlet} = 1.0 \times 10^4$ and $L_z^+|_{inlet} = 5.5 \times 10^2$, respectively. Here, the ratios of present residence time in the computational domain, $T_{residence} = L_x/U_e$, and integral time for ensemble average of turbulence statistics $T_{integral}$ to the relaxation time λ are presented in table 2. Even at $We = 100$, the residence time is a factor of four larger than the relaxation time. For all of the cases, the present integral time is much larger than the relaxation time.

In the driver part, the computational domain and grid size are $(100\theta_0 \times 30\theta_0 \times 20\pi\theta_0/3)$ and $(128 \times 64 \times 64)$, respectively. The present turbulence statistics are obtained by averaging over space (spanwise direction) and time of over $2000\theta_0/U_e$ after the turbulent flow becomes stationary, where the time increment $\Delta tU_e/\theta_0$ is 0.008 for the FENE-P model and 0.02 for Newtonian fluid. In this paper, $\overline{\ }$ and $'$ represent the time–space (spanwise direction) average and the deviation, respectively. The superscript $^+$ represents the spanwise- and time averaged local variables normalized by wall variables. The superscript $^{++}$ represents values scaled by inner variables

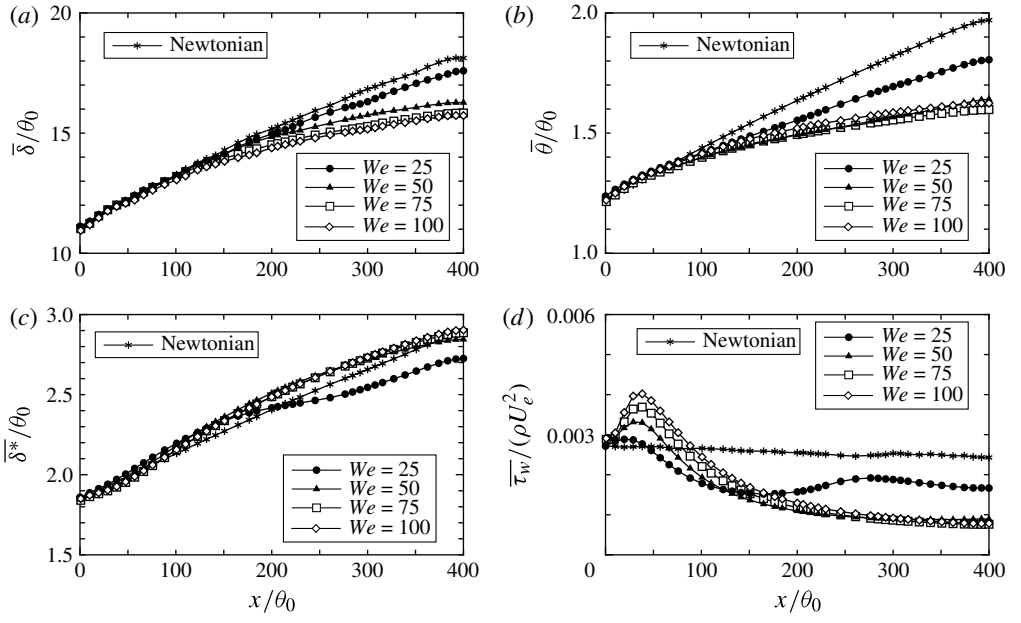

FIGURE 1. Streamwise variations in (*a*) boundary layer thickness $\overline{\delta}/\theta_0$, (*b*) momentum thickness $\overline{\theta}/\theta_0$, (*c*) displacement thickness $\overline{\delta^*}/\theta_0$, (*d*) wall-shear stress $\overline{\tau_w}/(\rho U_e^2)$.

without spatial and time average, i.e. with the local value of wall shear stress. In this study, the Schmidt number Sc is fixed at $Sc = 0.2$, which gives a constant artificial diffusivity of $1/(ScRe_{\theta_0}) = 0.01$. For comparison, Dimitropoulos *et al.* (2005, 2006) used $1/(ScRe_{\theta_0}) = 1$, but only applied at locations where the conformation tensor lost positive definiteness. It is known that this type of artificial diffusive term smears the steep gradient of polymer stresses unlike the local artificial diffusivity scheme (see Min, Yoo & Choi 2001; Dubief *et al.* 2005), but it should not affect the physical interpretation of the results (e.g. Sureshkumar & Beris 1995; Sureshkumar *et al.* 1997; Dimitropoulos *et al.* 1998; Ptasinski *et al.* 2003; Li *et al.* 2006; Kim *et al.* 2007; Xi & Graham 2010*a*).

4. Results

4.1. *Boundary layer parameters and drag reduction ratio*

Figures 1(*a*)–(*d*) show the streamwise variations in boundary layer thickness $\overline{\delta}/\theta_0 (= \overline{\delta}_{99.5}/\theta_0)$, momentum thickness $\overline{\theta}/\theta_0$, displacement thickness $\overline{\delta^*}/\theta_0$, and wall-shear stress $\overline{\tau_w}/(\rho U_e^2)$, respectively. The streamwise development of $\overline{\delta}/\theta_0$ is suppressed more with the increase in We, and $\overline{\delta}/\theta_0$ at $We = 75$ and 100 are almost identical. The value of $\overline{\theta}/\theta_0$ at $We = 50$–100 is strongly suppressed, while at $We = 25$ it is between the Newtonian and higher We cases. The value of $\overline{\delta^*}/\theta_0$ at $We = 50$–100 is larger in the downstream region compared with the Newtonian fluid, while at $We = 25$ it is smaller than that for the Newtonian fluid. The behaviour of $\overline{\theta}/\theta_0$ and $\overline{\delta^*}/\theta_0$ is directly related to the shape factor $H = \delta^*/\theta$ (see figure 2*a* later). At $We = 50$–100, the wall shear stress $\overline{\tau_w}/(\rho U_e^2)$ increases near the inlet region and monotonically decreases, while at $We = 25$, $\overline{\tau_w}/(\rho U_e^2)$ oscillates in the downstream region, in which its value is still smaller than that of Newtonian fluid. The $\overline{\tau_w}/(\rho U_e^2)$ corresponds to the friction

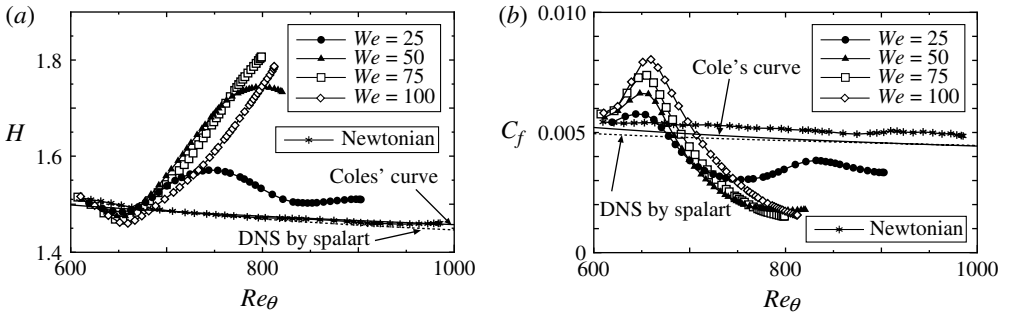

FIGURE 2. Boundary layer development: (*a*) shape factor *versus* Reynolds number and (*b*) friction coefficient *versus* momentum–thickness Reynolds number.

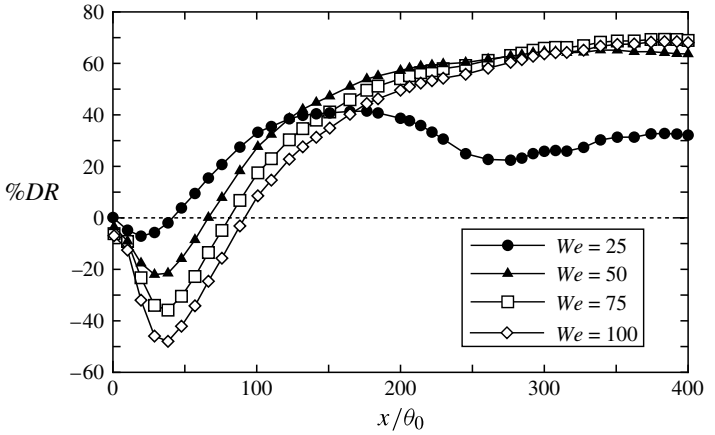

FIGURE 3. Streamwise variation in drag reduction ratio.

coefficient $C_f = \overline{\tau_w}/(\rho U_e^2/2)$ (see figure 2*b*), and this behaviour is closely related to the drag reduction ratio (see figure 3).

Figures 2(*a*) and 2(*b*) show the dependence of the shape factor H and skin friction coefficient C_f on the momentum–thickness Reynolds number Re_θ, which is useful for comparison with experimental data. In these figures, the solid and dotted lines represent Coles' curves (Coles 1962) and DNS data obtained by Spalart (Spalart 1988), respectively. The data of H for Newtonian fluid agree well with Coles' curves and DNS data of Spalart, while the data of C_f is somewhat larger. This may be due to the effect of grid resolution as mentioned in § 3. However, the trend of C_f is consistent with the Coles' curves and the value is within a 10 % tolerance. It should be noted that even in the spectral DNS of Newtonian flows, it is not only the actual values of C_f that differ, but also inconsistent trends with respect to Re_θ (see Schlatter & Örlü 2010).

As the Reynolds number increases, the value of H at $We = 25$–100 first decreases near the inlet region, and then drastically increases from $Re_\theta \simeq 650$ to the outlet plane (figure 2*a*). The increase in H versus Re_θ observed here is consistent with the previous experimental study on the drag-reducing turbulent boundary layer flow in cationic and non-ionic surfactant solutions (see Itoh *et al.* 2005; Tamano *et al.* 2009*b*, 2010). It should be noted that at $We = 25$, H oscillates in the downstream region, and at

$We = 50$, it has a maximum around $Re_\theta = 800$. The value of C_f increases with the increase in Re_θ for $Re_\theta \lesssim 650$, after the maximum it decreases. At $We = 25$, C_f oscillates in the streamwise direction. The behaviour of C_f is consistent with that of H. The comparison of C_f with Newtonian fluid is discussed by estimating the drag reduction ratio (see figure 3).

Figure 3 shows the streamwise variation in the drag reduction ratio DR for the four values of We studied here. This ratio is defined as follows:

$$DR(x) = \frac{C_{f\,Newtonian}(x) - C_{f\,Viscoelastic}(x)}{C_{f\,Newtonian}(x)}, \tag{4.1}$$

where $C_{f\,Newtonian}(x)$ and $C_{f\,Viscoelastic}(x)$ are the skin friction coefficients for Newtonian and viscoelastic fluids, which are functions of the streamwise position x. The drag-reducing effect shifts downstream with the increasing We. It can be concluded that the streamwise profile of DR shifts downstream with the increase in the relaxation time, since the other rheological parameters and the Reynolds number are constant. The level of DR at $We = 25$ is much smaller than those of $We = 50$ and higher, which is consistent with the previous DNSs (Dimitropoulos *et al.* 2005; Tamano *et al.* 2009*a*). At $We = 50$–100, the DR becomes larger in the streamwise direction, and seems to saturate at more than 60 %. On the other hand, at $We = 25$, the region of DR is below $\sim$40 %, and oscillates with downstream position: the first maximum is at $x/\theta_0 \simeq 150$, the minimum is at $x/\theta_0 \simeq 260$, and a second slight maximum is at $x/\theta_0 \simeq 380$.

In the inlet region, the negative DR is due to the sudden change of velocity fields caused by the unrealistic effect of the inlet boundary condition in which the velocity field data of Newtonian fluid in the driver part are used directly (see Dimitropoulos *et al.* 2005, 2006; Tamano *et al.* 2007, 2009*a*).

4.2. *Turbulence statistics*

Figure 4(*a–d*) show the wall-normal profiles of mean (spanwise and time averaged) velocity, U^+, at different streamwise locations. In these figures, the linear profile $U^+ = y^+$, the log-law profile ($U^+ = 2.44 \ \ln y^+ + 5.0$) and the Virk ultimate profile (Virk 1975) ($U^+ = 11.7 \ln y^+ - 17$) are also shown. At $We = 25$, U^+ shifts upward compared with the Newtonian log-law. On the other hand, at $We = 50$ and higher, U^+ shifts upward more and increases with the increase in x, i.e. the increase in DR, and the slope is much larger than that of the Newtonian log-law. The present DNS results are consistent with previous experiments (e.g. Warholic *et al.* 1999*a*; Itoh *et al.* 2005; Tamano *et al.* 2009*b*) and DNS (e.g. Dimitropoulos *et al.* 2005; Tamano *et al.* 2009*a*). At $We = 75$ and 100, the mean velocities at $x/\theta_0 = 392.2$ agree well with the Virk ultimate profile.

Figure 5 shows profiles of streamwise turbulence intensity, u'^+_{rms}, at $We = 25$–100. At $We = 25$, except in the upstream region where the DR is negative, u'^+_{rms} is larger than that from the DNS by Spalart (1988) for Newtonian fluid, and the maximum becomes larger in the streamwise direction. The wall-normal location of the maximum is slightly farther from the wall. At $We = 50$, the maximum of u'^+_{rms} in the downstream region is much larger than that of the Newtonian fluid, over 1.5 times larger at $x/\theta_0 = 392.2$. At $We = 75$, the maximum of u'^+_{rms} (outside the upstream region) becomes larger in the streamwise direction, as in the case of $We = 50$, but the maxima near the wall are much smaller compared with those of $We = 50$, and the plateau region appears around $y^+ = 100$, which is not detected in $We = 25$ and 50. At $We = 100$, the streamwise turbulence intensity is strongly attenuated across the boundary layer (figure 5*d*), and the maximum of u'^+_{rms} shows somewhat complex

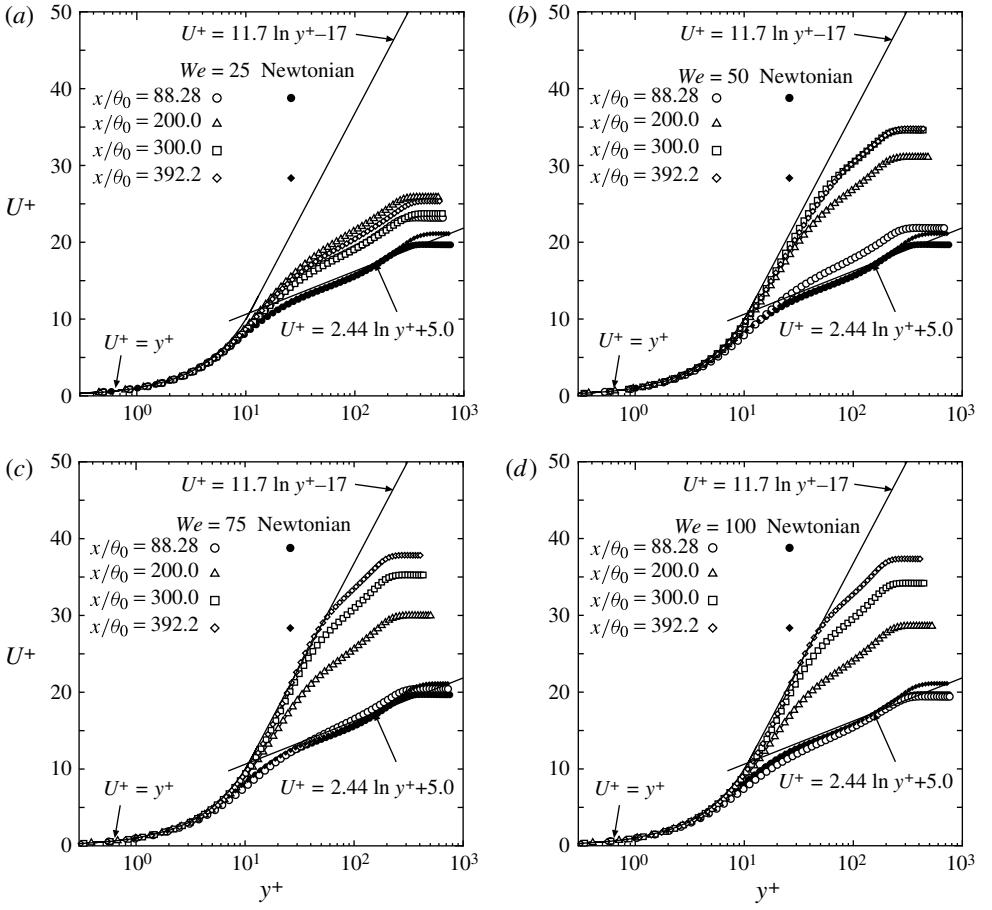

FIGURE 4. Profiles of streamwise mean velocity in wall units: (*a*) $We = 25$, (*b*) $We = 50$, (*c*) $We = 75$ and (*d*) $We = 100$.

behaviour. This observation is related to the phase difference between streamwise profiles of the drag reduction ratio and streamwise turbulence intensity as further discussed below (see figure 9*c* for details).

Figure 5(*d*) also shows that at $We = 100$ a second maximum appears around $y^+ = 200$, and the second maximum values are almost independent of the streamwise location. This second peak rises due to the strong suppression of u'^+_{rms} in the log layer and seems to be consistent with experimental measurements on drag-reduced turbulent boundary layer for dilute cationic surfactant solutions, in which the second peak is observed near the centre of the boundary layer (see Itoh *et al.* 2005; Tamano *et al.* 2009*b*). These authors claimed that the second peak is due to the formation of the shear-induced structure (SIS), which is strongly related to the viscoelasticity and the drag-reducing ability in the turbulent flow of the dilute cationic surfactant solution. However, the second peak here may be due to long relaxation time, since the present DNS does not take the structure modification such as the SIS into account. Thus, further investigations are needed to understand the origin of the second peak of the streamwise turbulence intensity.

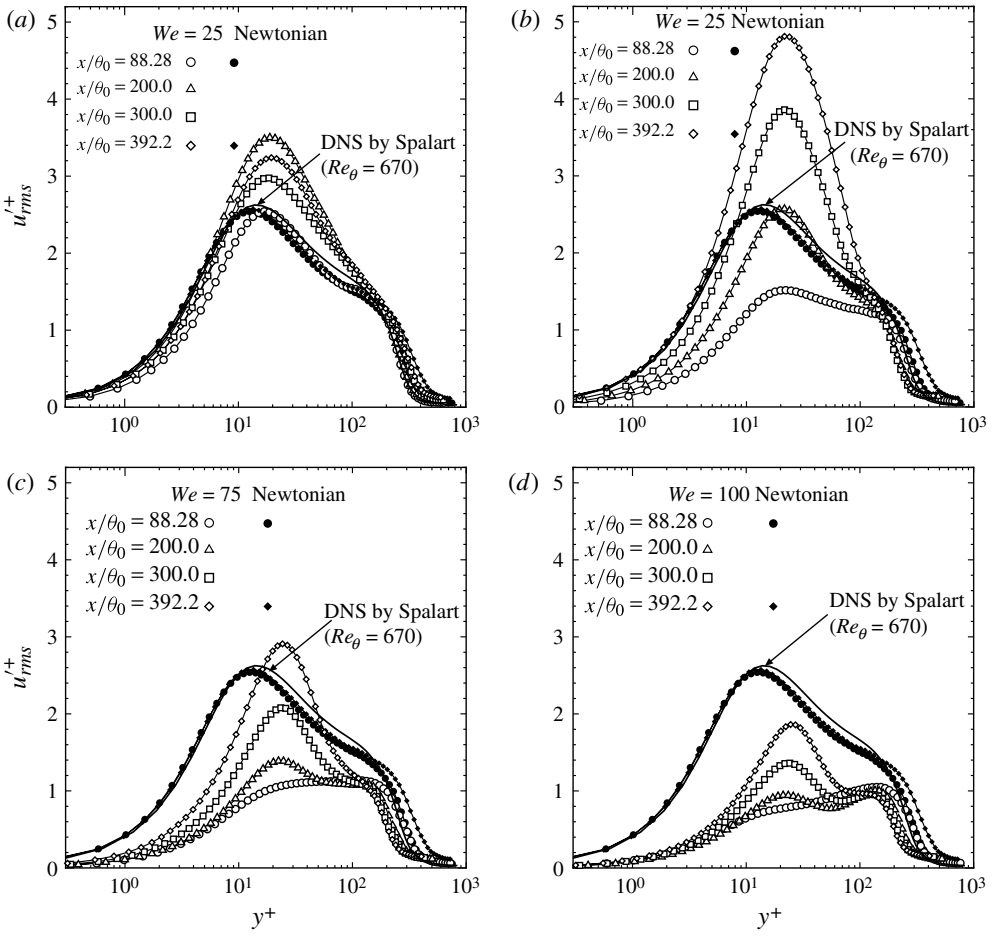

FIGURE 5. Profiles of streamwise turbulence intensity in wall units: (*a*) $We = 25$, (*b*) $We = 50$, (*c*) $We = 75$ and (*d*) $We = 100$.

Figure 6 shows distributions of the wall-normal turbulence intensity v'^{+}_{rms} in wall units. For all of the cases of We, the wall-normal turbulence intensity v'^{+}_{rms} is smaller than that for the Newtonian fluid. At the same streamwise location, the maximum of v'^{+}_{rms} becomes smaller with the increase in We. At $We = 75$ and 100, the maxima of v'^{+}_{rms} are almost half those of the Newtonian fluid. The maxima of v'^{+}_{rms} also move away from the wall; the maxima at $We = 50$–100 are located at $y^{+} \simeq 200$, while the maximum at $We = 25$ is located at $y^{+} \simeq 100$.

Figure 7 shows distributions of the Reynolds shear stress $-\overline{u'v'}^{+}$. At $We = 25$, $-\overline{u'v'}^{+}$ is slightly smaller than that of Newtonian fluid. As a whole, $-\overline{u'v'}^{+}$ decreases with the increase in We. At $We = 75$ and 100, the Reynolds shear stress is weak across the boundary layer in the downstream region. This is consistent with experimental results that the Reynolds shear stress is very small at large drag reduction ratios for wall-bounded turbulent flows (see e.g. Warholic *et al.* 1999*a*,*b*; Kawaguchi *et al.* 2002; Itoh *et al.* 2005; Tamano *et al.* 2009*b*).

Figure 8 shows profiles of trace of the conformation tensor, $\overline{C_{kk}}/L^2$. The maximum of $\overline{C_{kk}}/L^2$ in the region of $10 < y^{+} < 30$ indicates that turbulence statistics are strongly

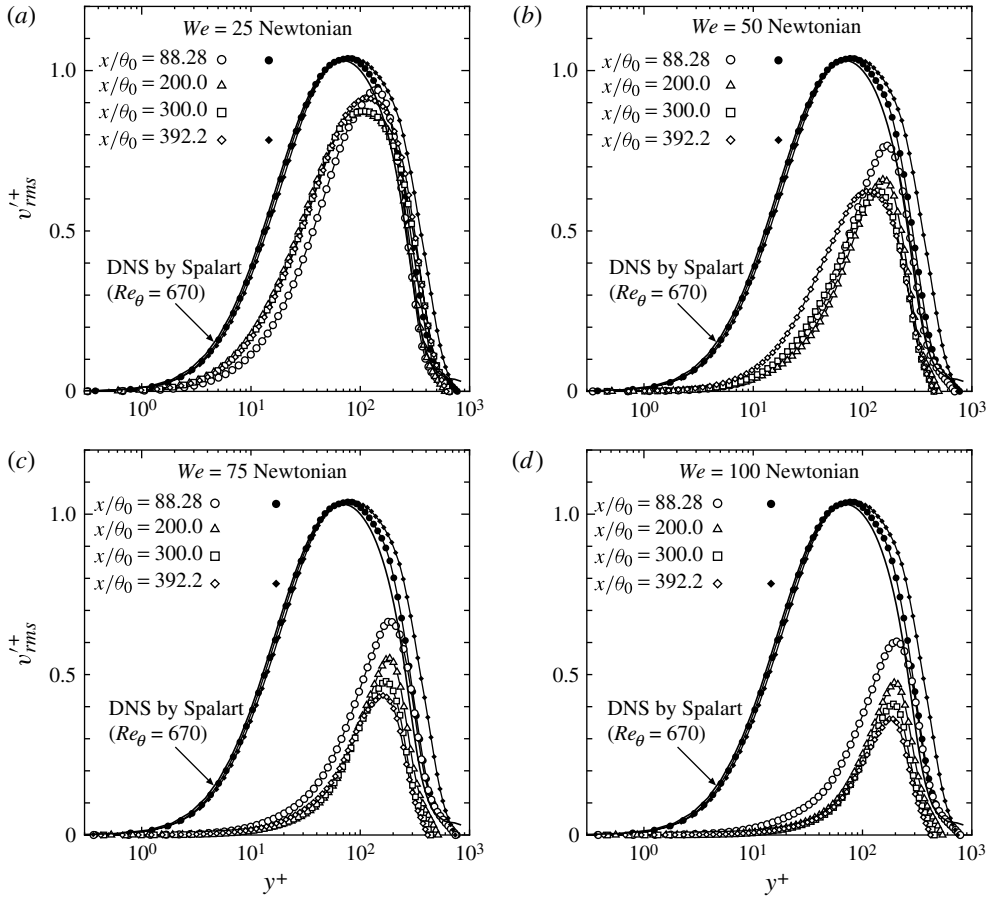

FIGURE 6. Profiles of wall-normal turbulence intensity in wall units: (*a*) $We = 25$, (*b*) $We = 50$, (*c*) $We = 75$ and (*d*) $We = 100$.

affected in the buffer layer by the high elongational viscosity. The value of $\overline{C_{kk}}/L^2$ is almost zero in the region away from the wall. At the same streamwise location, the $\overline{C_{kk}}/L^2$ becomes larger with the increase in *We*.

Next, we investigate streamwise profiles of turbulence statistics at $y^+ = 30$, since both their modification and the polymer elongation are largest in the vicinity of this value, as observed above. Figure 9(*a–e*) show streamwise variations in the mean velocity, trace of conformation tensor, streamwise turbulence intensity, wall-normal turbulence intensity and Reynolds shear stress, respectively. In figure 9(*a*), solid and dashed lines represent Virk and Newtonian log-laws, respectively. For the Newtonian fluid, mean velocities scaled by the friction velocity at $y^+ = 30$, $U^+|_{y^+=30}$ are almost constant and slightly smaller than the Newtonian log-law in the whole computational domain. For viscoelastic fluids, near the inlet region, $U^+|_{y^+=30}$ decreases in the streamwise direction, and has a minimum. This corresponds to the region of negative drag reduction and is again due to the inlet condition. Downstream of this region at $We = 25$ $U^+|_{y^+=30}$ has a maximum at $x/\theta_0 \simeq 150$ and a slight minimum at $x/\theta_0 \simeq 270$, and slightly increases again. At $We = 50$, $U^+|_{y^+=30}$ has a slight maximum in the region of $250 \leqslant x/\theta_0 \leqslant 300$. At $We = 75$ and 100, $U^+|_{y^+=30}$ gradually increases and reaches

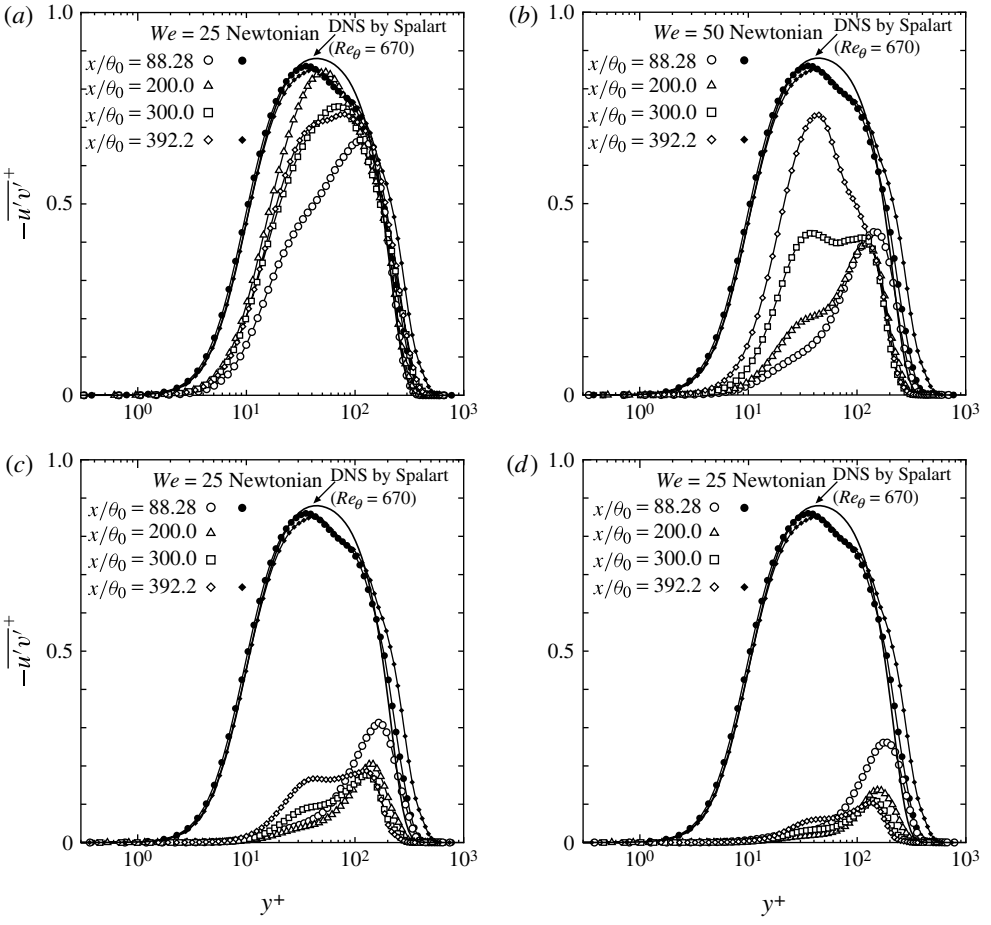

FIGURE 7. Profiles of Reynolds shear stress in wall units: (*a*) $We = 25$, (*b*) $We = 50$, (*c*) $We = 75$ and (*d*) $We = 100$.

the Virk log-law value. Streamwise profiles of $U^+|_{y^+=30}$ are similar with those of drag reduction ratio DR (cf. figures 9*a* and 3).

Figure 9(*b*) shows that the maximum of $\overline{C_{kk}}|_{y^+=30}/L^2$, which is observed near $x/\theta_0 = 50$, increases with the increase in We. Note that streamwise locations of maxima of $\overline{C_{kk}}|_{y^+=30}/L^2$ correspond to locations of minima of DR. Downstream of such maxima, at $We = 25$, $\overline{C_{kk}}|_{y^+=30}/L^2$ has a slight minimum at $x/\theta_0 \simeq 180$ and a slight maximum at $x/\theta_0 \simeq 300$. At $We = 50$, 75, 100, $\overline{C_{kk}}|_{y^+=30}/L^2$ decreases in the streamwise direction, while $U^+|_{y^+=30}$ or DR increases. This indicates that once polymers are strongly stretched in the upstream region, which results in the high extensional viscosity, large viscoelastic stress is not necessary for the large DR in the downstream region. We elaborate on this observation below. It is also reminiscent of the observation by Xi & Graham (2010*b*) in minimal channel flow that during intervals of 'hibernation', in which the level of drag reduction is highest, the polymer chains are relaxing. That is, what occurs temporally in the minimal channel is similar to what occurs spatially in boundary layer flow. The connection between these observations is particularly close in the $We = 25$ case, where the level of drag reduction displays

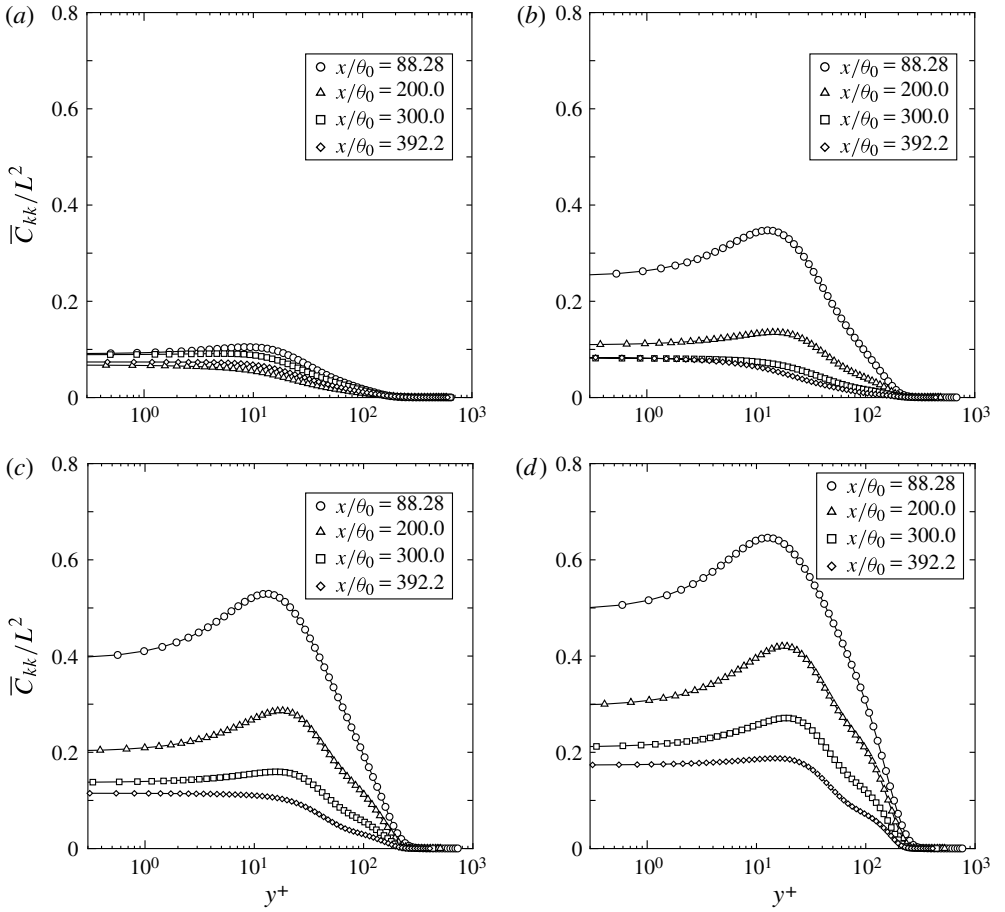

FIGURE 8. Profiles of trace of conformation tensor: (*a*) $We = 25$, (*b*) $We = 50$, (*c*) $We = 75$ and (*d*) $We = 100$.

both a maximum, at $x/\theta_0 \approx 160$, and a minimum, at $x/\theta_0 \approx 260$. The level of polymer stretching has corresponding extrema a short distance downstream, i.e. a minimum at $x/\theta_0 \approx 180$ and a maximum at $x/\theta_0 \approx 280$. The present result is also consistent with the DNS of Dimitropoulos *et al.* (2005) and the experiment of Hou *et al.* (2008).

It can be observed that the streamwise profile shifts downstream as *We* increases (figure 9*c*). At $We = 25$, the streamwise location at which $u'^+_{rms}|_{y^+=30}$ of viscoelastic fluids becomes larger than that of Newtonian fluid shifts downstream compared with the streamwise location at which the *DR* becomes positive. The same behaviour is observed at $We = 50$ and higher. Moreover, such phase difference between *DR* and $u'^+_{rms}|_{y^+=30}$ increases with the increase in *We*, i.e. the relaxation time λ. The lack of correspondence of *DR* and $u'^+_{rms}|_{y^+=30}$ observed here is consistent with the first DNS of Dimitropoulos *et al.* (2005) who reported that the phase difference between polymer stretch and vortex damping increased with *We*.

Figure 9(*d*) shows that the wall-normal turbulence intensity at $y^+ = 30$, $v'^+_{rms}|_{y^+=30}$, sharply decreases as *We* increases. At $We = 25$, $v'^+_{rms}|_{y^+=30}$ starts to increase at $x/\theta_0 \simeq 100$, reaches the maximum at $x/\theta_0 \simeq 230$ and then slightly decreases in the streamwise

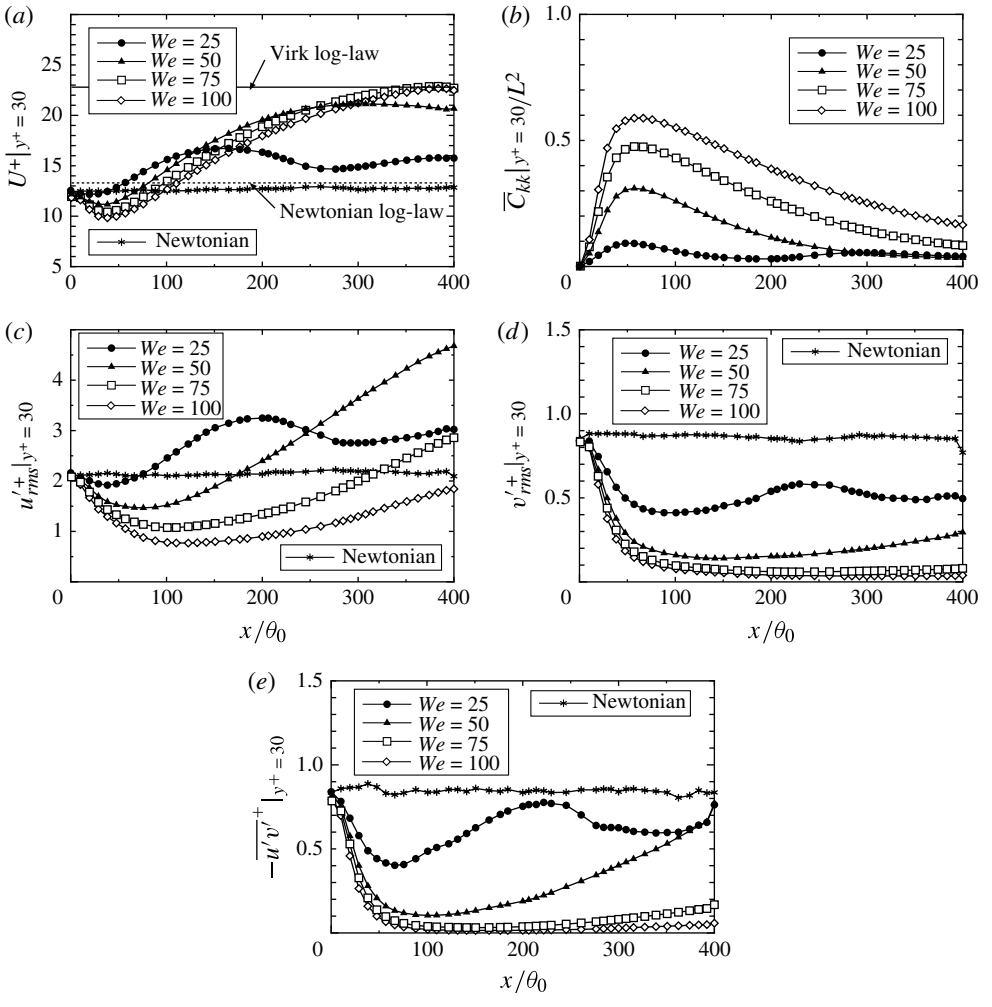

FIGURE 9. Streamwise variations at $y^+ = 30$: (*a*) mean velocity, (*b*) trace of conformation tensor, (*c*) streamwise turbulence intensity, (*d*) wall-normal turbulence intensity and (*e*) Reynolds shear stress.

direction. At $We = 50$, $v'^+_{rms}|_{y^+=30}$ gradually increases from $x/\theta_0 \simeq 200$, while at $We = 75$ and 100, it very slightly increases from around $x/\theta_0 = 350$–380, respectively. The streamwise profiles of $v'^+_{rms}|_{y^+=30}$ seem to be shifted more downstream compared with those of $u'^+_{rms}|_{y^+=30}$. This can be seen for example by the fact that the maximum of $v'^+_{rms}|_{y^+=30}$ is more downstream than that of $u'^+_{rms}|_{y^+=30}$.

Figure 9(*e*) shows the Reynolds shear stress $-\overline{u'v'}^+|_{y^+=30}$. Its qualitative behaviour is similar to that of $v'^+_{rms}|_{y^+=30}$. At $We = 100$, the $-\overline{u'v'}^+|_{y^+=30}$ is very small in $100 < x/\theta_0 < 200$, and is slightly increasing with downstream distance. The small value of the Reynolds shear stress has been reported in experimental studies on drag-reducing cationic surfactant solutions (see e.g. Warholic *et al.* 1999*b*; Kawaguchi *et al.* 2002; Itoh *et al.* 2005; Tamano *et al.* 2009*b*) and polymer solutions (Warholic *et al.* 1999*a*).

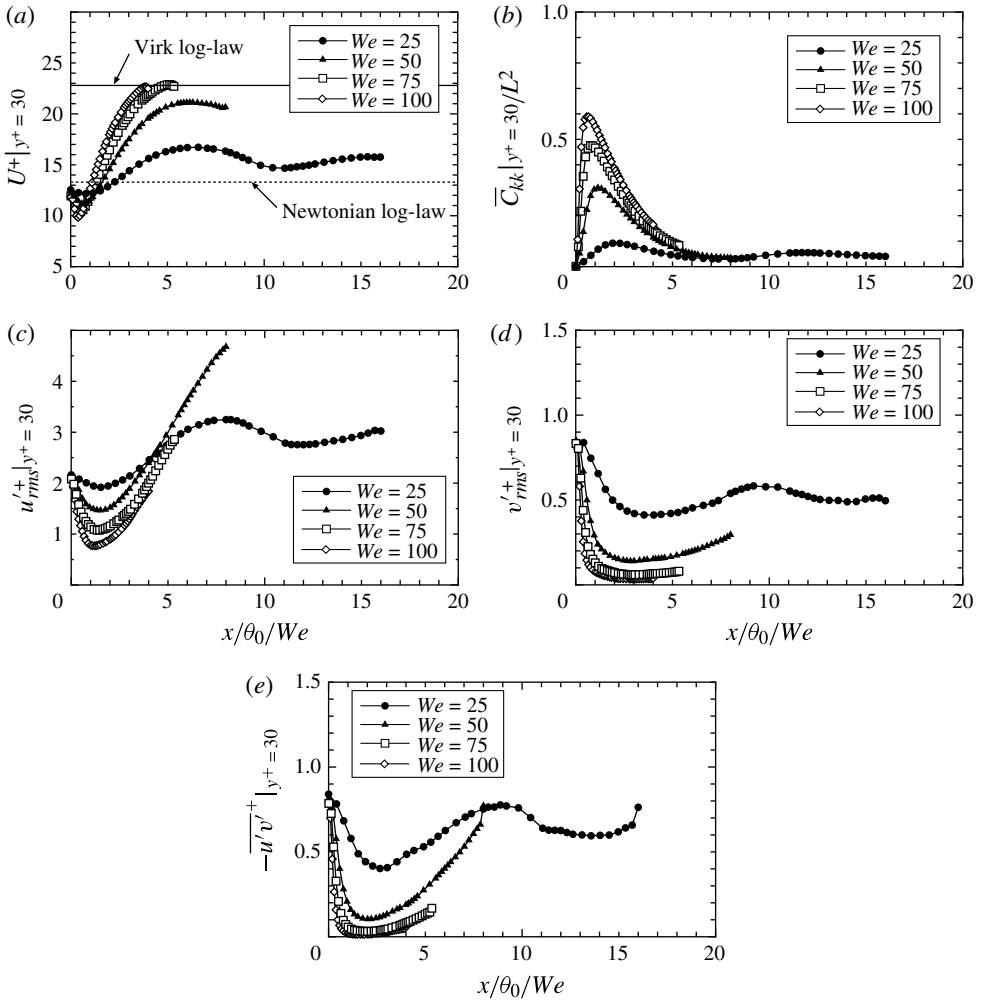

FIGURE 10. Streamwise variations at $y^+ = 30$, abscissa as $x/\theta_0/We$ instead of x/θ_0: (*a*) mean velocity, (*b*) trace of conformation tensor, (*c*) streamwise turbulence intensity, (*d*) wall-normal turbulence intensity and (*e*) Reynolds shear stress.

Comparing streamwise variations among the drag reduction ratio *DR*, trace of conformation tensor, and turbulence statistics (cf. figures 3 and 9), it is revealed that the trace of conformation tensor, i.e. the magnitude of polymer elongation is anticorrelated with *DR*. On the other hand, compared with the streamwise profile of *DR*, streamwise profiles of streamwise and wall-normal turbulence intensities and the Reynolds shear stress shift downstream, and the phase difference becomes larger with the increase in *We*, in which the phase difference from *DR* is largest for the wall-normal intensity and is smallest for the streamwise turbulence intensity.

To clarify the dependence on the relaxation time λ of the streamwise variations of turbulence statistics, the abscissa in figure 9, x/θ_0, is replaced by $x/\theta_0/We$ in figure 10. With this change, we are measuring downstream distance in length travelled per polymer relaxation time. When viewed this way it is seen that the variations in streamwise and wall-normal turbulence intensities and the Reynolds shear stress at

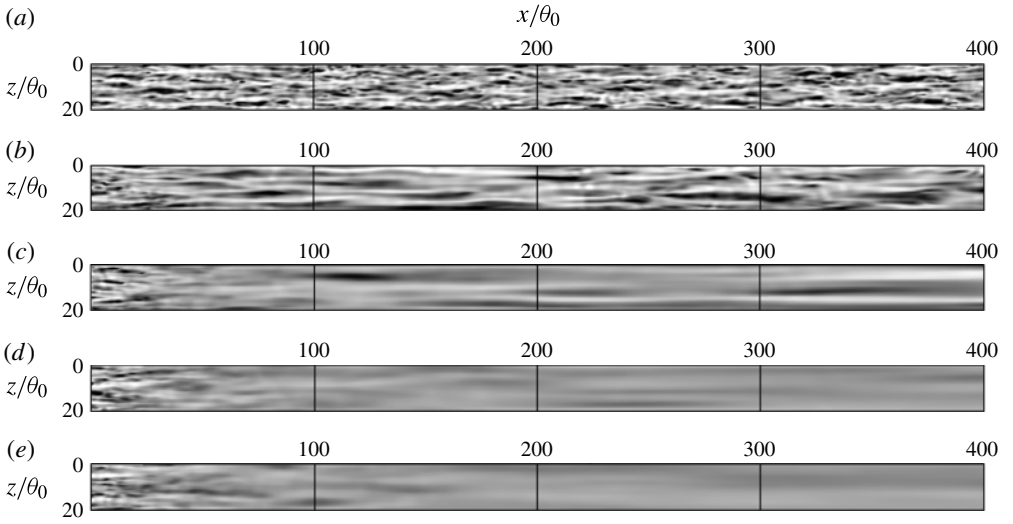

FIGURE 11. Contour of local wall-shear stress fluctuations ($-0.8 \leqslant \tau_w''/\overline{\tau_w}^z \leqslant 0.8$, white to black): (*a*) Newtonian, (*b*) $We = 25$, (*c*) $We = 50$, (*d*) $We = 75$ and (*e*) $We = 100$.

different We are comparable, unlike in figure 9. In particular, the positions of the extrema on figure 10 display a much weaker dependence on We than on figure 9. This observation indicates that the phase difference observed here is mainly due to the difference in the relaxation time.

4.3. *Correlations between stress, velocity and polymer conformation*

The results above show a general trend of the level of drag reduction (or, equivalently, the mean velocity at $y^+ = 30$) increasing while the polymer stress decreases. As noted, this observation is generally consistent both with some previous work on boundary layers (Dimitropoulos *et al.* 2005) and the observations of Xi & Graham (2010*b*) in minimal channel flow, although the present results are somewhat influenced by the artificial inlet boundary condition. In this section we examine in more detail the relationship between wall shear stress, velocity and polymer conformation.

Figure 11 shows instantaneous contours of local wall-shear stress fluctuation $\tau_w'' = \tau_w - \overline{\tau_w}^z$ scaled by $\overline{\tau_w}^z$. Black and white contours represent high and low wall-shear stress regions, respectively. For the Newtonian fluid, many small high and low wall-shear stress regions appear. On the other hand, at $We = 25$, high and low wall-shear stress regions show larger scales. At $We = 50$, some high wall-shear stress regions are observed and the instantaneous wall-shear stress is almost homogeneous in the downstream region. At $We = 75$ and 100, the local wall-shear stress is almost uniform except in the upstream region, where the influence of the artificial inlet boundary condition is large.

To examine the relationships between velocity, wall-shear stress and polymer conformation in more detail, we present in figure 12 joint probability density functions (JPDFs) of instantaneous wall-shear stress $\tau_w/(\rho U_e^2)$ and streamwise velocity scaled by friction velocity U^{++} at wall normal position $y^{++} = 30$ in the whole computational domain. Figure 12(*a–c*) reveal that the correlation between $\tau_w/(\rho U_e^2)$ and $U^{++}|_{y^{++}=30}$ is negative, and the strongest correlation is observed around the Newtonian log-law line for the Newtonian fluid, in the region between the Virk and Newtonian log-

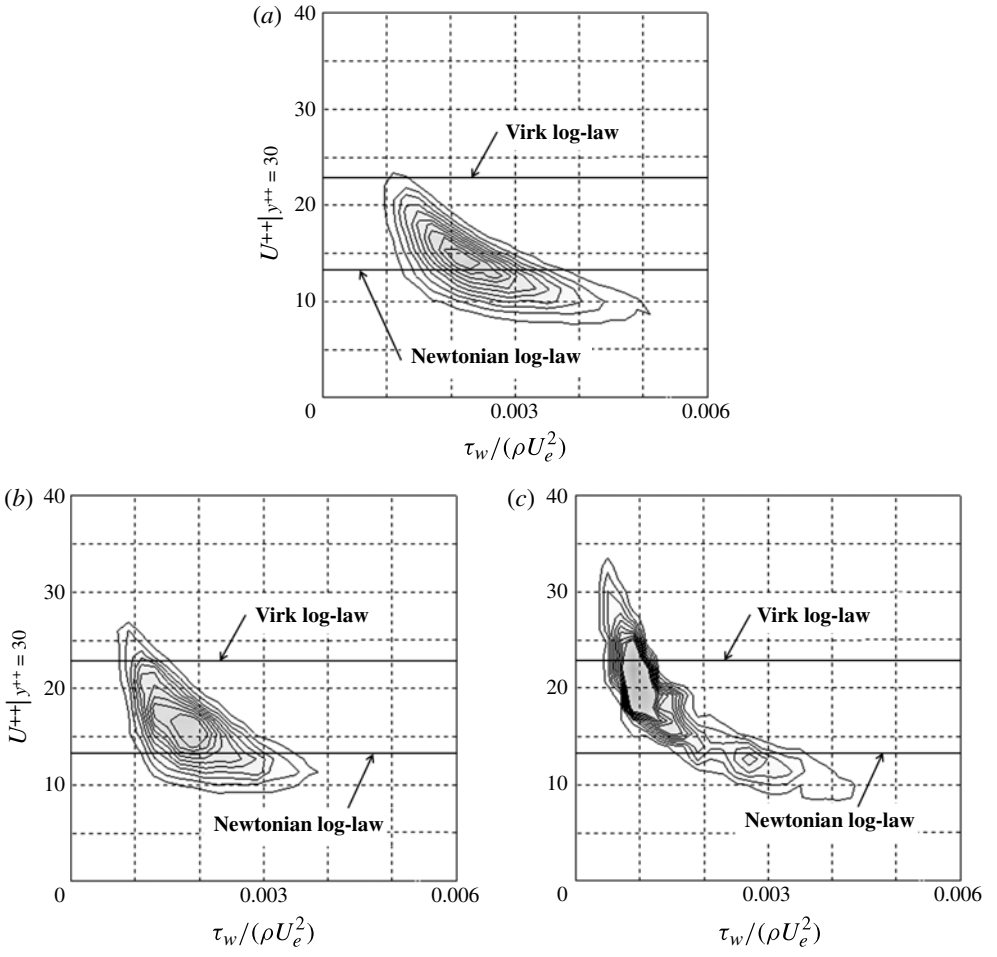

FIGURE 12. Joint probability density functions of instantaneous wall-shear stress and streamwise velocity scaled by friction velocity at $y^{++} = 30$ in the whole computational domain: (*a*) Newtonian, (*b*) $We = 25$ and (*c*) $We = 50$.

law lines at $We = 25$, and around the Virk log-law line at $We = 50$. Figure 13 shows JPDFs of instantaneous trace of conformation tensor $\overline{C_{kk}}/L^2$ at $y^{++} = 30$ and $U^{++}|_{y^{++}=30}$ in the whole computational domain. The negative correlation between $C_{kk}|_{y^{++}=30}/L^2$ and $U^{++}|_{y^{++}=30}$ is observed at both $We = 25$ and 50. Figure 14 shows JPDFs of instantaneous wall-shear stress $\tau_w/(\rho U_e^2)$ and trace of conformation tensor $\overline{C_{kk}}/L^2$ at $y^{++} = 30$ in the whole computational domain. One can confirm the positive correlation between $\tau_w/(\rho U_e^2)$ and $C_{kk}|_{y^{++}=30}/L^2$ at both $We = 25$ and 50, which is consistent with the finding that $U^{++}|_{y^{++}=30}$ is negatively correlated to both $C_{kk}|_{y^{++}=30}/L^2$ and $\tau_w/(\rho U_e^2)$.

Figure 15 shows values of $U^{++}|_{y^{++}=30}$ versus $\tau_w/(\rho U_e^2)$ at a particular time instant at $z = 3L_z/4$, i.e. along a line oriented in the streamwise direction. For the Newtonian case, these 'trajectories' show movement with a negative correlation over a wide range of $U^{++}|_{y^{++}=30}$ and $\tau_w/(\rho U_e^2)$. At $We = 25$, the trajectories are confined to a smaller range of $\tau_w/(\rho U_e^2)$. At $We = 50$, the range of $U^{++}|_{y^{++}=30}$ is almost the same as in the

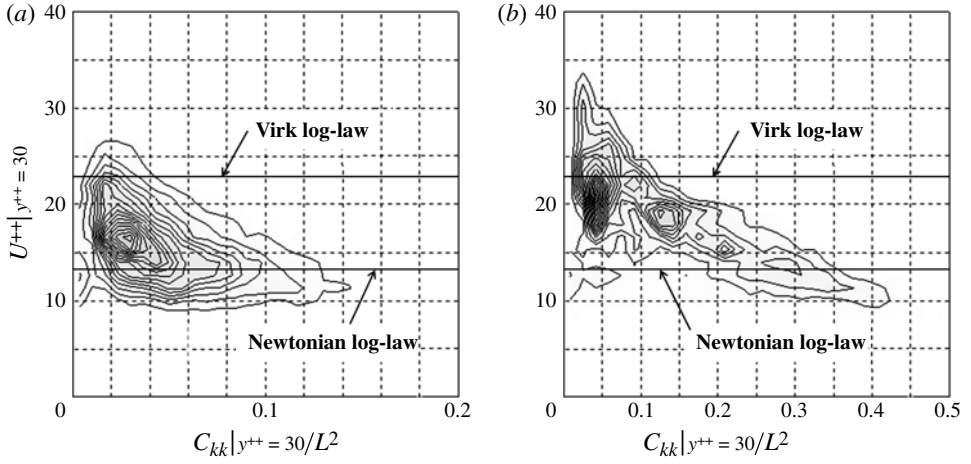

FIGURE 13. Joint probability density functions of instantaneous trace of conformation tensor and streamwise velocity scaled by friction velocity at $y^{++} = 30$ in the whole computational domain: (*a*) $We = 25$ and (*b*) $We = 50$. Note the change in the horizontal axis scale between the two plots.

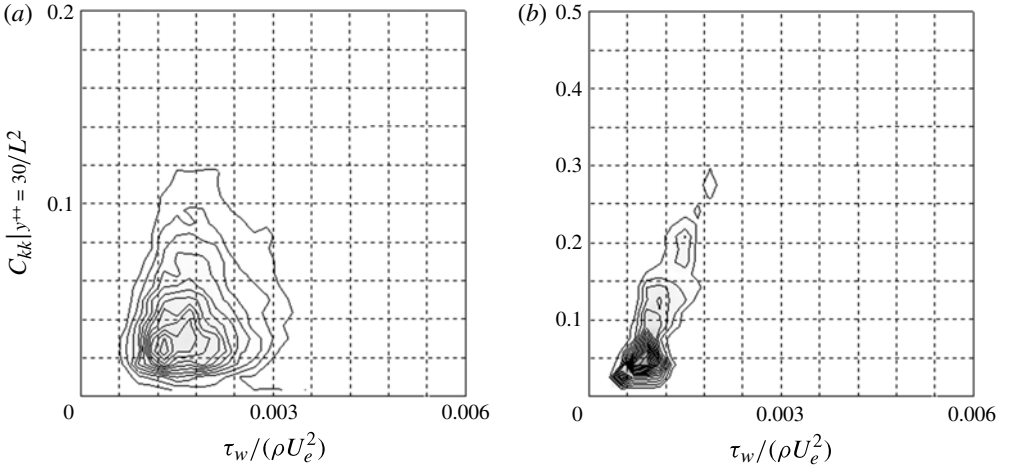

FIGURE 14. Joint probability density functions of instantaneous wall-shear stress and trace of conformation tensor at $y^{++} = 30$ in the whole computational domain: (*a*) $We = 25$ and (*b*) $We = 50$.

Newtonian case, but there is much less (spatial) fluctuation. Figure 16 shows values of $U^{++}|_{y^{++}=30}$ versus $C_{kk}|_{y^{++}=30}/L^2$ as a function of x at $z = 3L_z/4$. It is found that at $We = 50$ the movement is less and the range is wider than at $We = 25$.

The results presented here clearly indicate a local negative correlation between the level of drag reduction (mean velocity) and polymer stress, and are again consistent with the presence of the active and hibernating turbulence mechanism in the turbulent boundary layer flow.

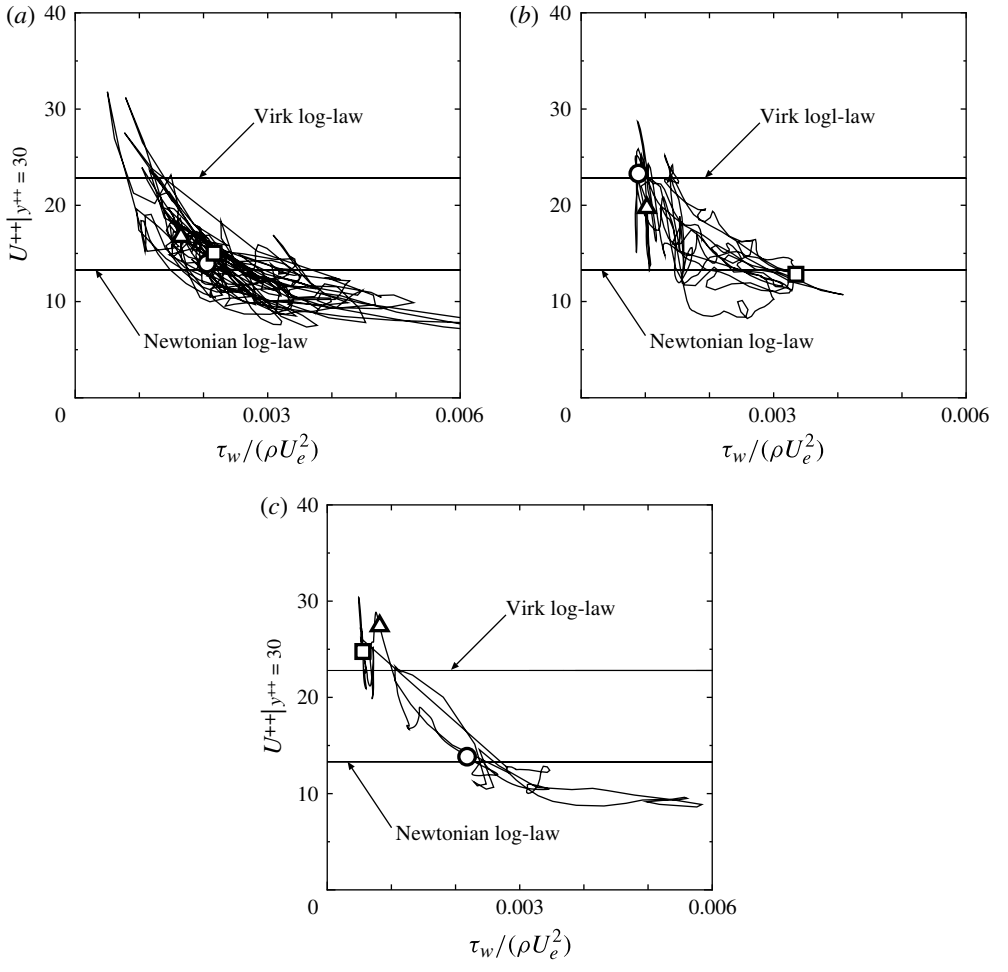

FIGURE 15. Instantaneous values of $U^{++}|_{y^{++}=30}$ *versus* $\tau_w/(\rho U_e^2)$ as a function of x at $z = 3L_z/4$: (*a*) Newtonian, (*b*) $We = 25$ and (*c*) $We = 50$. Symbols ◯, △ and □ illustrate the values at $x/\theta_0 = 100$, 200 and 300, respectively.

4.4. *Effect of removal of polymer stresses in downstream region*

To further examine the role of the viscoelastic stresses in the downstream evolution of the level of drag reduction, we performed simulations at $We = 100$ in which the viscoelastic stresses were set to zero beyond a fixed downstream distance b. Two values of b were tested: $b = 100\theta_0$, where the polymer stretching and turbulence intensity are large and the level of drag reduction is slightly negative (because of the inlet conditions), and $b = 200\theta_0$, where the polymer stress is still substantial but the level of drag reduction is high. The removal of the stresses was implemented by multiplying them by the damping function,

$$W(x) = \frac{1}{2}\left[1 - \frac{\tanh\left\{\dfrac{\alpha(x-b)}{(1-2b)x+b}\right\}}{\tanh(\alpha)}\right], \tag{4.2}$$

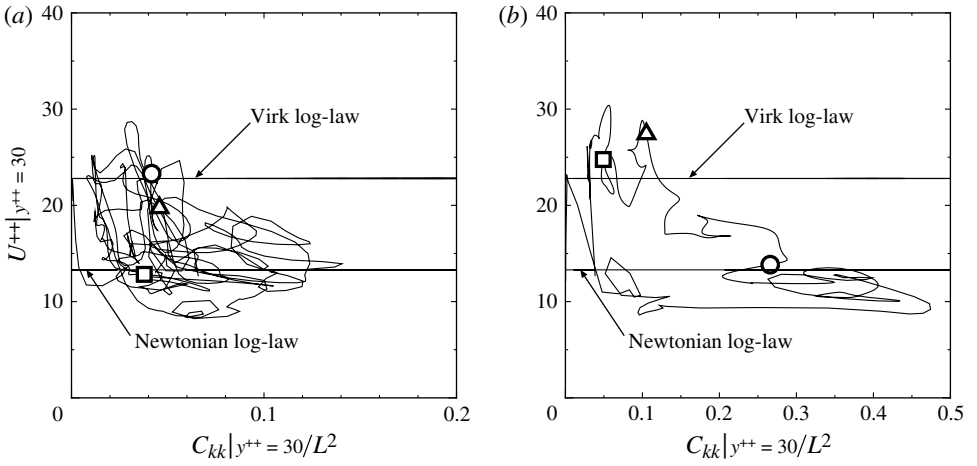

FIGURE 16. Instantaneous values of $U^{++}|_{y^{++}=30}$ *versus* $C_{kk}|_{y^{++}=30}/L^2$ as a function of x at $z = 3L_z/4$: (*a*) $We = 25$ and (*b*) $We = 50$. Symbols ◯, △ and □ illustrate the values at $x/\theta_0 = 100$, 200 and 300, respectively.

where α is fixed at 50. All other numerical and physical conditions are the same as in the previous sections.

Figure 17(*a–f*) show the streamwise dependence of the trace of conformation tensor $\overline{C_{kk}}|_{y^+=30}/L^2$, the drag reduction ratio DR, the mean velocity $U^+|_{y^+=30}$, the streamwise and wall-normal turbulence intensities $u'^+_{rms}|_{y^+=30}$ and $v'^+_{rms}|_{y^+=30}$, and the Reynolds shear stress $-\overline{u'v'}^+|_{y^+=30}$ in these cases.

Consider first the case of damping at $x/\theta_0 = 100$. The streamwise profile of DR starts to depart from the profile without damping at $x/\theta_0 = 80$ and reaches a maximum around $x/\theta_0 = 130$, in which the value is more than twice the value of DR without damping at the same streamwise location (figure 17*b*). The sudden change of the momentum balance (removal of the polymer contribution to the shear stress) causes the large drag reduction around $x/\theta_0 = 130$, which corresponds to the maximum of $U^+|_{y^+=30}$ (see also figure 17*c*).

After the maximum, the level of DR drastically decreases, becoming negative and almost constant in the region of $280 \leqslant x/\theta_0 \leqslant 400$ (figure 17*b*). This rapid reversion to essentially normal Newtonian turbulence does not seem to be linked to outer region dynamics as these are hardly affected at all by the polymer dynamics. This point is illustrated in figure 18, which suggests that the difference in outer region turbulence statistics with and without damping is small.

Now consider the case of damping at $x/\theta_0 = 200$, where there is already a substantial degree of drag reduction. As in the above case, there is a slight increase in the level of drag reduction due to removal of the polymer shear stresses, but in contrast to that case, the level of drag reduction now remains high in the remainder of the domain. Similarly, $U^+|_{y^+=30}$ with damping at $x/\theta_0 = 200$ is larger than without damping (cf. figures 17*b* and 17*c*). These results support the hypothesis that once the flow has been driven by polymer stretching into a regime with substantial drag reduction, the viscoelastic stress is not necessary for the drag reduction to persist for a substantial distance in the downstream region. (Of course, one expects that in a sufficiently long domain the flow would eventually revert

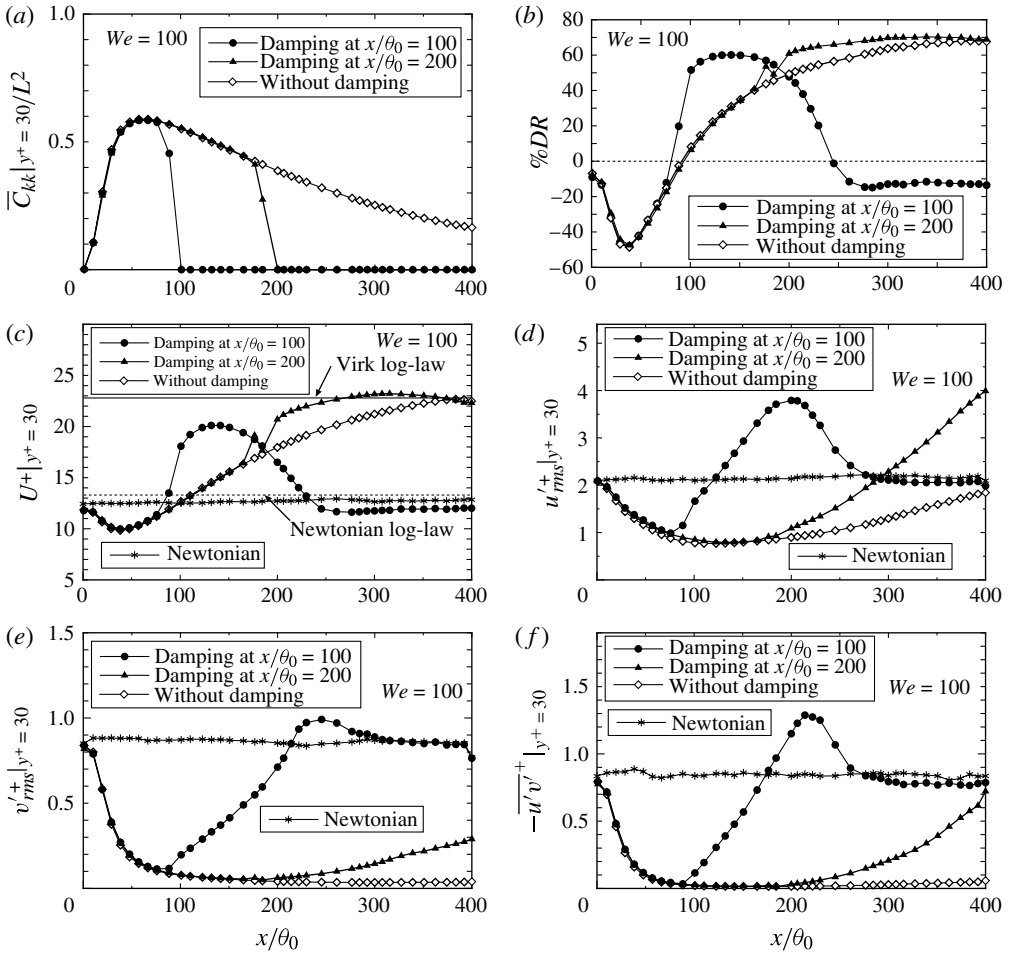

FIGURE 17. Streamwise variations at $We = 100$ with damping at $x/\theta_0 = 100$ and 200: (*a*) trace of conformation tensor, (*b*) drag reduction ratio, (*c*) mean velocity, (*d*) streamwise turbulence intensity, (*e*) wall-normal turbulence intensity and (*f*) Reynolds shear stress.

back to conventional Newtonian turbulence.) Analogous results were found in the minimal channel simulations of Xi & Graham (2010*b*). They observed that once the a viscoelastic simulation had begun to enter a hibernation interval, the polymer stresses could be turned off and the flow would continue to hibernate for several eddy turnover times, exhibiting for example the same transient approach to the Virk log-law slope found in the fully viscoelastic case.

Values of $u'^{+}_{rms}|_{y^+=30}$, $v'^{+}_{rms}|_{y^+=30}$ and $-\overline{u'v'}^{+}|_{y^+=30}$ with damping at $x/\theta_0 = 100$ have maxima at $x/\theta_0 = 200$, 250 and 220, respectively, which are much larger than in the Newtonian case, and then decrease to the outlet plane. At $x/\theta_0 > 300$, they are almost constant and $u'^{+}_{rms}|_{y^+=30}$ and $-\overline{u'v'}^{+}|_{y^+=30}$ are slightly smaller than that in the Newtonian case. On the other hand, with damping at $x/\theta_0 = 200$, the $u'^{+}_{rms}|_{y^+=30}$, $v'^{+}_{rms}|_{y^+=30}$ and $-\overline{u'v'}^{+}|_{y^+=30}$ increase monotonically from $x/\theta_0 \simeq 180$ to the outlet plane, at which $u'^{+}_{rms}|_{y^+=30}$ is almost twice that of Newtonian fluid, while $v'^{+}_{rms}|_{y^+=30}$ and $-\overline{u'v'}^{+}|_{y^+=30}$ are still smaller than those of Newtonian fluid. These increases in the

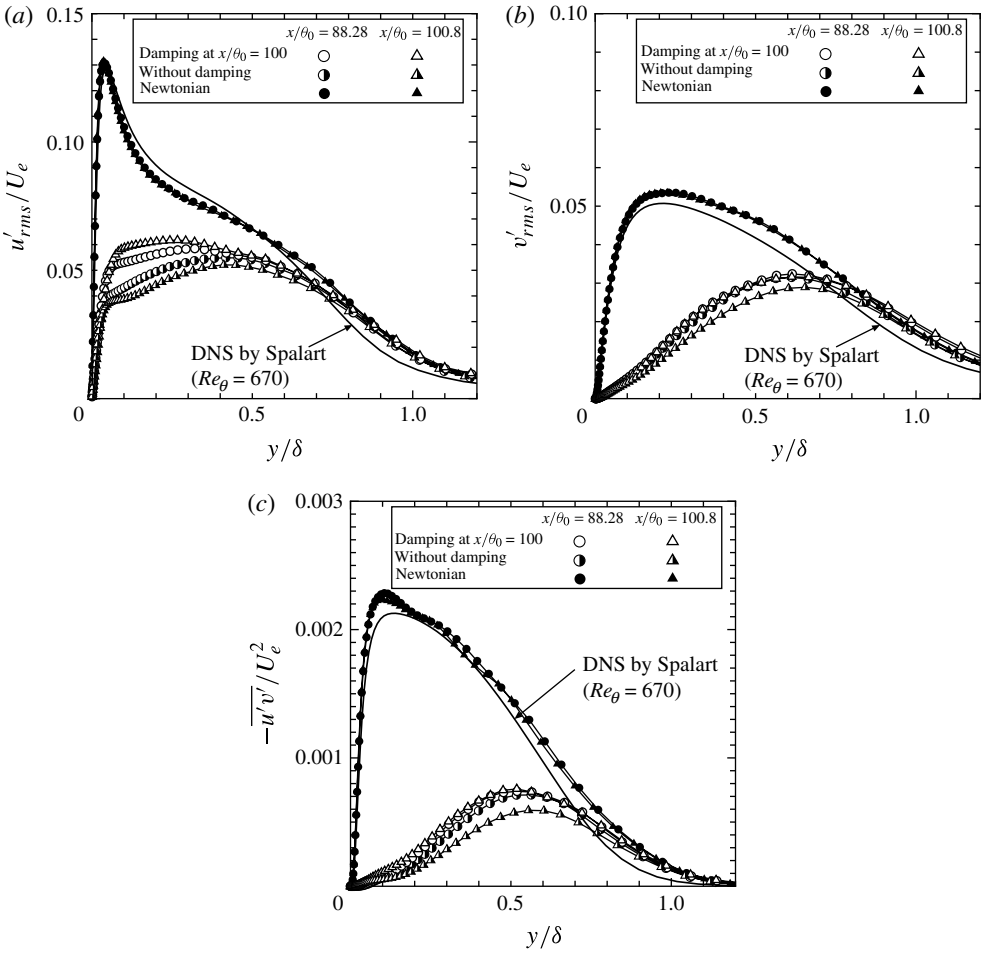

FIGURE 18. Wall-normal profiles of turbulence statistics with outer scaling at $We = 100$ with damping at $x/\theta_0 = 100$: (*a*) streamwise turbulence intensity, (*b*) wall-normal turbulence intensity and (*c*) Reynolds shear stress.

velocity fluctuations are consistent with expectation mentioned above that far enough downstream, the turbulence will revert to normal.

5. Conclusions

DNS of a zero-pressure gradient drag-reducing turbulent boundary layer of a viscoelastic fluid were performed at the momentum–thickness Reynolds number $Re_{\theta_0} = 500$ and Weissenberg numbers $We = 25,\ 50,\ 75$ and 100 using the FENE-P model with the maximum chain extensibility parameter $L^2 = 10\,000$ and the ratio of solvent viscosity to zero shear rate solution viscosity $\beta = 0.9$. An important limitation of the present study (as with many previous studies of boundary layer flow) is the artificial inlet condition. This condition leads to substantial transient stretching of the polymers and correspondingly to a negative level of drag reduction in the upstream region of the flow. (This condition is somewhat similar to the case of injecting polymers into an established turbulent boundary layer.) On the other

hand, most of the key qualitative results of this work arise from observations of the dynamics well downstream of this region, as well as trends with increasing *We* that are expected to be independent of the details of the upstream conditions. Key observations include the following. As *We* increases, i.e. the relaxation time becomes longer, the streamwise profile of *DR* shifts downstream. Here *DR* increases with the streamwise location, while the trace of conformation tensor decreases. More generally, the trace of conformation tensor, i.e. the magnitude of polymer elongation is spatially anticorrelated with *DR*, while in terms of streamwise and wall-normal turbulence intensities and the Reynolds shear stress, the phase difference from *DR* becomes larger with the increase in *We*, in which such the difference is largest and smallest for the wall-normal and streamwise turbulence intensities, respectively. The relationship between polymer stretching, velocity and wall shear stress was further illustrated by examination of joint probability density functions of instantaneous values of these quantities. These results shed further light on the spatial anticorrelation between polymer stretching and drag reduction as well as showing a related anticorrelation between the mean velocity at the edge of the log layer and the wall shear stress. Finally, by performing simulations in which the polymer stress is set to zero beyond a given downstream position, it is shown that high levels of drag reduction can be maintained for some distance downstream in the absence of polymer stress.

These results are consistent with recent observations by Xi & Graham (2010*b*) in minimal channel flow of viscoelastic fluids, and suggest that an important role for viscoelasticity in the turbulent drag reduction phenomenon, at least near solid surfaces, is to suppress conventional turbulence, while leaving behind a much weaker form of turbulence that can persist for a substantial length of time (or downstream distance) even in the absence of viscoelastic stresses.

This work was carried out under the Excellent Young Researchers Overseas Visit Program of the Japan Society for the Promotion of Science. It was partially supported by a Grant-in-Aid for Scientific Research (grant numbers 18360087 and 21760126) from the Japan Society for the Promotion of Science. MDG acknowledges the support of the National Science Foundation (grant number CBET-1066223).

REFERENCES

BENZI, R., DE ANGELIS, E. & L'VOV, V. S. 2006 Maximum drag reduction asymptotes and the cross-over to the Newtonian plug. *J. Fluid Mech.* **551**, 185–195.

BIRD, R. B., ARMSTRONG, R. C. & HASSAGER, O. 1987*a* *Dynamics of Polymeric Liquids. Volume 1: Fluid Mechanics*, 2nd edn. Wiley.

BIRD, R. B., ARMSTRONG, R. C. & HASSAGER, O. 1987*b* *Dynamics of Polymeric Liquids. Volume 2: Kinetic Theory*, 2nd edn. Wiley.

COLES, D. E. 1962 A manual of experimental boundary-layer practice for low-speed flow. *Rand Report*, No. R-403-PR, The Rand Corp., Santa Monica, CA.

DE ANGELIS, E., CASCIOLA, C. M. & PIVA, R. 2002 DNS of wall turbulence: dilute polymers and self-sustaining mechanisms. *Comput. Fluids* **31**, 495–507.

DIMITROPOULOS, C. D., DUBIEF, Y., SHAQFEH, E. S. G. & MOIN, P. 2006 Direct numerical simulation of polymer-induced drag reduction in turbulent boundary layer flow of inhomogeneous polymer solutions. *J. Fluid Mech.* **566**, 153–162.

DIMITROPOULOS, C. D., DUBIEF, Y., SHAQFEH, E. S. G., MOIN, P. & LELE, S. K. 2005 Direct numerical simulation of polymer-induced drag reduction in turbulent boundary layer flow. *Phys. Fluids* **17**, 011705.

DIMITROPOULOS, C. D., SURESHKUMAR, R. & BERIS, A. N. 1998 Direct numerical simulation of viscoelastic turbulent channel flow exhibiting drag reduction: effect of the variation of rheological parameters. *J. Non-Newtonian Fluid Mech.* **79**, 433–468.

DUBIEF, Y., TERRAPON, V., WHITE, C. M., SHAQREH, E. G., MOIN, P. & LELE, S. K. 2005 New answers on the interaction between polymers and vortices in turbulent flows. *Flow Turbul. Combust.* **74**, 311–329.

DUBIEF, Y., WHITE, C. M., TERRAPON, V. E., SHAQFEH, E. S. G., MOIN, P. & LELE, S. K. 2004 On the coherent drag-reducing and turbulence-enhancing behaviour of polymers in wall flows. *J. Fluid Mech.* **514**, 271–280.

DUBIEF, Y., WHITE, C. M., SHAQFEH, E. S. G. & TERRAPON, V. E. 2011 Polymer maximum drag reduction: a unique transitional state. *Center for Turbulence Research Annual Research Briefs 2010* 47–56.

DUKOWICZ, J. K. & DVINSKY, A. S. 1992 Approximate factorization as a high order splitting for the implicit incompressible flow equations. *J. Comput. Phys.* **102**, 336–347.

HOU, Y., SOMANDEPALLI, V. S. R. & MUNGAL, M. G. 2008 Streamwise development of turbulent boundary-layer drag reduction with polymer injection. *J. Fluid Mech.* **597**, 31–66.

HOUSIADAS, K. D. & BERIS, A. N. 2004 An efficient fully implicit spectral scheme for DNS of turbulent viscoelastic channel flow. *J. Non-Newtonian Fluid Mech.* **122**, 243–262.

ITOH, M., TAMANO, S., YOKOTA, K. & NINAGAWA, M. 2005 Velocity measurement in turbulent boundary layer of drag-reducing surfactant solution. *Phys. Fluids* **17**, 075107.

KAWAGUCHI, Y., SEGAWA, T., FENG, Z. & LI, P. 2002 Experimental study on drag-reducing channel flow with surfactant additives–spatial structure of turbulence investigated by PIV system. *Intl J. Heat Fluid Flow* **23**, 700–709.

KIM, K., ADRIAN, R. J., BALACHANDAR, S. & SURESHKUMAR, R. 2008 Dynamics of hairpin vortices and polymer-induced turbulent drag reduction. *Phys. Rev. Lett.* **100**, 134504.

KIM, K., LI, C.-F., SURESHKUMAR, R., BALACHANDAR, S. & ADRIAN, R. J. 2007 Effects of polymer stresses on eddy structures in drag-reduced turbulent channel flow. *J. Fluid Mech.* **584**, 281–299.

LI, C.-F., SURESHKUMAR, R. & KHOMAMI, B. 2006 Influence of rheological parameters on polymer induced turbulent drag reduction. *J. Non-Newtonian Fluid Mech.* **140**, 23–40.

LI, W. & GRAHAM, M. D. 2007 Polymer induced drag reduction in exact coherent structures of plane Poiseuille flow. *Phys. Fluids* **19**, 083101.

LUND, T. S., WU, X. & SQUIRES, K. D. 1998 Generation of turbulent inflow data for spatially-developing boundary layer simulations. *J. Comput. Phys.* **140**, 233–258.

MIN, T., YOO, J. Y. & CHOI, H. 2001 Effect of spatial discretization schemes on numerical solutions of viscoelastic fluid flows. *J. Non-Newtonian Fluid Mech.* **100**, 27–47.

PROCACCIA, I., L'VOV, V. S. & BENZI, R. 2008 Colloquium: theory of drag reduction by polymers in wall-bounded turbulence. *Rev. Mod. Phys.* **80**, 225–247.

PTASINSKI, P. K., BOERSMA, B. J., NIEUWSTADT, F. T. M., HULSEN, M. A., VAN DEN BRULE, B. H. A. A. & HUNT, J. C. R. 2003 Turbulent channel flow near maximum drag reduction: simulations, experiments and mechanisms. *J. Fluid Mech.* **490**, 251–291.

SCHLATTER, P. & ÖRLÜ, R. 2010 Assessment of direct numerical simulation data of turbulent boundary layers. *J. Fluid Mech.* **659**, 116–126.

SPALART, P. R. 1988 Direct simulation of a turbulent boundary layer up to $Re_\theta = 1410$. *J. Fluid Mech.* **187**, 61–98.

SREENIVASAN, K. R. & WHITE, C. M. 2000 The onset of drag reduction by dilute polymer additives, and the maximum drag reduction asymptote. *J. Fluid Mech.* **409**, 149–164.

STONE, P. A., ROY, A., LARSON, R. G., WALEFFE, F. & GRAHAM, M. D. 2004 Polymer drag reduction in exact coherent structures of plane shear flow. *Phys. Fluids* **16**, 3470–3482.

STONE, P. A., WALEFFE, W. & GRAHAM, M. D. 2002 Toward a structural understanding of turbulent drag reduction: nonlinear coherent states in viscoelastic shear flow. *Phys. Rev. Lett.* **89**, 208301.

SURESHKUMAR, R. & BERIS, A. N. 1995 Effect of artificial stress diffusivity on the stability of numerical calculations and the flow dynamics of time-dependent viscoelastic flows. *J. Non-Newtonian Fluid Mech.* **60**, 53–80.

SURESHKUMAR, R., BERIS, A. N. & HANDLER, R. A. 1997 Direct numerical simulation of the turbulent channel flow of a polymer solution. *Phys. Fluids* **9**, 743–755.

TAMANO, S., ITOH, M., HOSHIZAKI, K. & YOKOTA, K. 2007 Direct numerical simulation on the drag-reducing turbulent boundary layer of viscoelastic fluid. *Phys. Fluids* **19**, 075106.

TAMANO, S., ITOH, M., HOTTA, S., YOKOTA, K. & MORINISHI, Y. 2009*a* Effect of rheological properties on drag reduction in turbulent boundary layer flow. *Phys. Fluids* **21**, 055101.

TAMANO, S., ITOH, M., INOUE, T., KATO, K. & YOKOTA, K. 2009*b* Turbulence statistics and structures of drag-reducing turbulent boundary layer in homogenous aqueous surfactant solutions. *Phys. Fluids* **21**, 045101.

TAMANO, S., ITOH, M., KATO, K. & YOKOTA, K. 2010 Turbulent drag reduction in nonionic surfactant solutions. *Phys. Fluids* **22**, 055102.

VAN DER VORST, H. A. 1992 Bi-CGSTAB: a fast and smoothly converging variant of BiCG for the solution of nonsymmetric linear systems. *SIAM J. Sci. Stat. Comput.* **13**, 631–644.

VIRK, P. S. 1975 Drag reduction fundamentals. *AIChE J.* **21** (4), 625–656.

WARHOLIC, M. D., MASSAH, H. & HANRATTY, T. J. 1999*a* Influence of drag-reducing polymers on turbulence: effect of Reynolds number, concentration and mixing. *Exp. Fluids* **27**, 461–472.

WARHOLIC, M. D., SCHMIDT, G. M. & HANRATTY, T. J. 1999*b* The influence of a drag-reducing surfactant on a turbulent velocity field. *J. Fluid Mech.* **388**, 1–20.

WHITE, C. M. & MUNGAL, M. G. 2008 Mechanics and prediction of turbulent drag reduction with polymer additives. *Annu. Rev. Fluid Mech.* **40**, 235–256.

WU, X. & MOIN, P. 2009 Direct numerical simulation of turbulence in a nominally zero-pressure-gradient fat-plate boundary layer. *J. Fluid Mech.* **630**, 5–41.

XI, L. & GRAHAM, M. D. 2010*a* Turbulent drag reduction and multistage transitions in viscoelastic minimal flow units. *J. Fluid Mech.* **647**, 421–452.

XI, L. & GRAHAM, M. D. 2010*b* Active and hibernating turbulence in minimal channel flow of Newtonian and polymeric fluids. *Phys. Rev. Lett.* **104**, 218301.

YU, B. & KAWAGUCHI, Y. 2003 Effect of Weissenberg number on the flow structure: DNS study of drag-reducing flow with surfactant additives. *Intl J. Heat Fluid Flow* **24**, 491–499.

YU, B. & KAWAGUCHI, Y. 2006 Parametric study of surfactant-induced drag-reduction by DNS. *Intl J. Heat Fluid Flow* **27**, 887–894.